# LADSDIn: LiCSAR-Based Anomaly Detector of Seismic Deformation in InSAR

Xianjian Shi ⬤ and Bin Pan ⬤

*Abstract*—**Manual analysis of LiCSAR deformation data in tectonic zones and timely detection of pre-earthquake anomalous activity are very time-consuming. To solve this problem, an LiCSAR-based anomaly detector of seismic deformation in interferometric synthetic aperture radar (LADSDIn) is constructed in this article. LADSDIn can automatically detect and extract anomalous activity and seismic deformation in tectonic zones. LADSDIn is modeled by learning the spatiotemporal characteristics of MTInSAR time series deformation data to detect abnormal deformation. The detector considers transients that deviate from the "predicted" deformation, which are considered "anomalous." For earthquake-prone regions, "anomalies" with outlier characteristics in spatial and temporal properties are usually the deformations caused by seismic activities. We successfully applied LADSDIn to January 8, 2022, Menyuan Mw 6.7 earthquake in China, and LADSDIn successfully detected the extent of ground deformation induced by this seismic activity. The results show that the deformation range of the ascending track is −350–87 mm, and the deformation range of the descending track is −127–132 mm. The detector successfully detected the "anomalous deformation" signs before the earthquake (November 2021). In addition, LADSDIn supports parallel processing in chunks to reduce computation time. The characteristics of LADSDIn facilitate cluster deployment and use for automatic detection and extraction of seismic deformation in global tectonic zones. This work provides theoretical support for the automation and refinement study of global seismic activity.**

*Index Terms*—**Automatic processing, deformation monitoring, earthquake, interferometric synthetic aperture radar, Sentinel-1.**

## I. INTRODUCTION

**G**ROUND deformation is the most direct apparent phenomenon of earthquake occurrence, and it is essential data for inversion of earthquake damage, epicenter mechanism, fault structure, etc. [1], [2]. In recent years, differential interferometric synthetic aperture radar (DInSAR) has been widely used in the study of earthquakes [3]. Compared with traditional geodetic methods, DInSAR technology has the features of all-weather, all-day, and no ground control in monitoring ground deformation [4], [5], [6].

Although DInSAR can effectively detect the slight deformation of the ground surface, the monitoring accuracy of DInSAR is affected by interference loss of coherence and atmospheric

delay, and the ground movement rate cannot exceed a certain threshold, so MTInSAR technology was born [7], [8]. MTInSAR is represented by persistent scatterer interferometric synthetic aperture radar (PSInSAR) and small baseline subset interferometric synthetic aperture radar (SBASInSAR) [9], [10]. PSInSAR performs phase modeling and deformation solving based on a discrete point set of PS points composed of highly coherent image elements. Ferretti et al. [11] used PSInSAR to extract landslide deformation rates and verified its ability to detect millimeter precision deformation. SBASInSAR improves coherence and deformation detection accuracy by limiting interference to spatial baselines using multiple master image combinations [12]. The combined approach of SBASInSAR can extract distributed point targets that remain coherent for a certain period, further increasing the point density, which is very suitable for natural ground deformation monitoring and can achieve long time series and millimeter-scale deformation monitoring at the regional scale [13].

However, the high price of commercial SAR data and the severe scarcity of civilian SAR data have limited the application of MTInSAR to seismic deformation studies for a long time [14]. The Sentienl-1 satellite launched by the European Space Agency breaks the mold [15]. Part of the Copernicus Project, Sentienl-1 consists of two satellites, each carrying a C-band synthetic aperture radar with an average revisit period of 12 days, and provides free all-weather, day, and night images of the Earth's surface to the general public [16].

As a game changer, the Sentienl-1 satellite has contributed significantly to the development of the global SAR industry [17], [18]. Sentinel-1 acquires up to 2000 SAR images daily, with a data capacity of even 10 TB [19], [20]. In this context, more and more scholars are using MTInSAR technology and Sentienl-1 data to carry out high-precision seismic deformation studies [21], [22], [23]. Due to the extensive range of ground deformation information, good continuity, and high deformation accuracy obtained by MTInSAR technology, the results of fault geometry parameter inversion and sliding distribution inversion are more comprehensive, detailed, and reliable [24], [25].

However, manual extraction of seismic deformation using the MTInSAR technique and Sentienl-1 data is very time-consuming [26]. During the deformation, decompression, coregistration, inversion, interferogram generation, and interferometric phase unwrapping occupy the entire processing time. To address this problem, Lazecký et al. [19] produced and made freely available the LiCSAR product based on super-computer clusters, SBASInSAR technology, and automatic
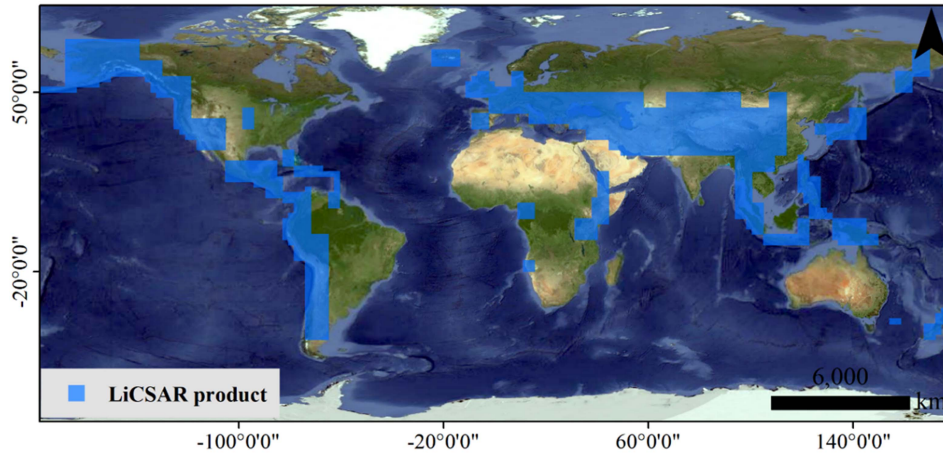
Fig. 1. Diagram of LiCSAR coverage range; the background image is a Google Earth image.

processing chains. LiCSAR is updated regularly, its products include geocoded unwrapped interferograms and coherence estimates, and LiCSAR covers major tectonics and volcanoes around the globe (see Fig. 1). Based on LiCSAR products, researchers can quickly acquire global tectonic and volcanic deformation [27]. MTInSAR has entered the era of Big Data high-performance computing [28].

China is an earthquake-prone country with many seismic zones and a high frequency of earthquakes. In total, 7% of China's territory endures 33% of the world's strongest earthquakes on the mainland, making it one of the most earthquake-prone countries in the world [29], [30], [31]. Although LiCSAR products cover the major seismic regions in China, manual analysis of LiCSAR deformation data in tectonic zones and timely detection of pre-earthquake anomalous activity are time-consuming and require staff with expertise in seismic and InSAR.

In this article, an LiCSAR-based anomaly detector of seismic deformation in InSAR (LADSDIn) is constructed to automatically detect and extract anomalous activity and seismic deformation in tectonic zones. The main contributions of this article are as follows.

1) A novel network architecture based on LiCSAR products and deep learning anomaly detection techniques is modeled by learning the spatiotemporal characteristics of MTInSAR time series deformation data to detect anomalous deformations.

2) LADSDIn is an automatic, deep-learning anomaly detector, and transient phenomena that deviate from the "expected" deformation are considered "anomalies." For earthquake-prone regions, "anomalies" that exhibit outlier characteristics in spatiotemporal properties are usually the deformations caused by seismic activity.

3) We propose a novel seismic deformation extraction strategy. The strategy first learns outlier features in time and the space of seismic deformation data. Then, it separates the seismic deformation from the background time series based on the learned outlier features from the labeled anomalies.

4) We successfully applied LADSDIn to the Mw 6.7 magnitude earthquake in Mengyuan, China, on January 8, 2022. LADSDIn successfully resolved the extent of ground deformation caused by seismic activity. In addition, LADSDIn supports parallel processing in chunks to reduce computation time. The characteristics of LADSDIn facilitate cluster deployment and use for automatic detection and extraction of seismic deformation in global tectonic zones.

## II. MATERIALS AND METHODS

### A. MTInSAR Deep Learning

Deep learning has been shown to be very effective in pattern recognition and feature extraction from high-dimensional data [32]. Traditional machine learning algorithms, such as support vector machines and random forests, rely on manually crafted features, require domain-specific knowledge, and are limited by the complexity of the data [33]. In contrast, deep learning models can automatically learn relevant features from the data and better handle large amounts of data, especially nonlinear and complex deformations, and these advantages can improve performance and reduce the need for domain-specific knowledge [34].

Earthquakes are vibrations caused by the rapid release of energy from the earth's crust. During this process, the dislocation and rupture of plates trigger ground deformation. Unlike "normal" deformation, the ground deformation caused by earthquakes is transient, i.e., the seismic deformation exhibits outlier characteristics in time. On the other hand, earthquake-induced ground deformation is usually a sudden uplift or sudden subsidence of a region, i.e., seismic deformation exhibits outlier characteristics over a large spatial scale. The low number of earthquakes in the long time series of deformation data makes the earthquake deformation extraction study more suitable for machine learning.

Based on the unique data structure of earthquakes, this article uses long short-term memory (LSTM) to learn the data features of MTInSAR to output "predicted" values, and deformations that deviate from "predicted" will be marked as abnormal deformations. Finally, the seismic deformations are filtered from
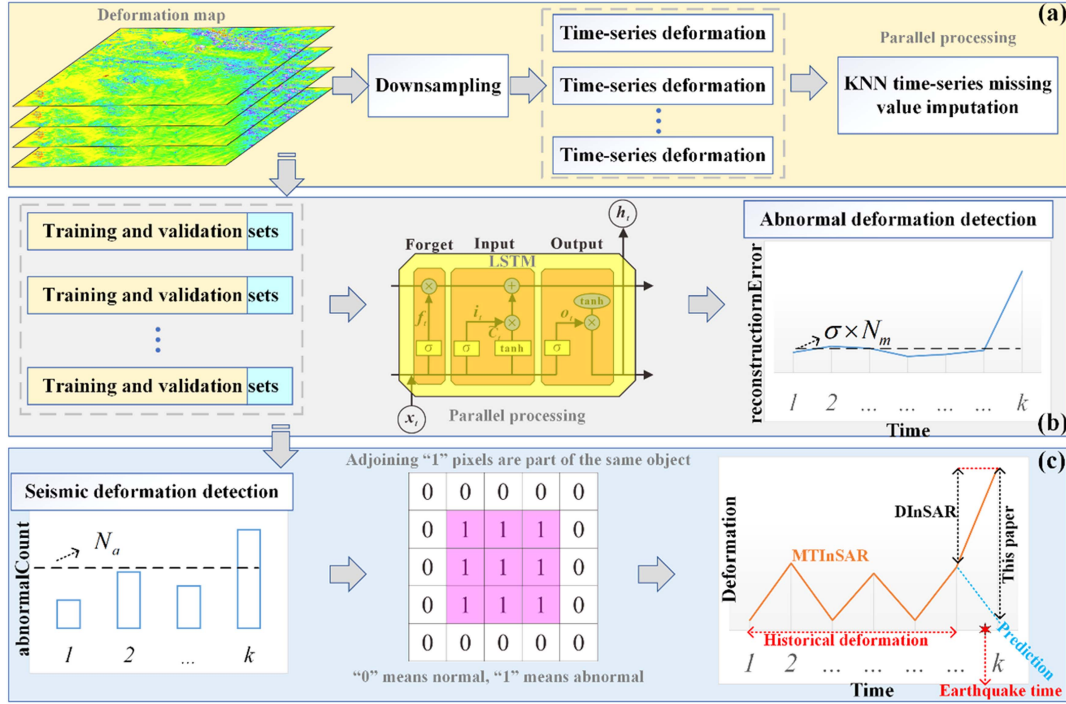
Fig. 2    General framework of LADSDIn.

the anomalous deformations based on the outlier characteristics of the seismic data. Fig. 2 shows the general framework of LADSDIn. The detector consists of the following three modules.

1) *Data cleaning module*. This module is used to uniformly sample the LiCSAR deformation results and determine whether there are missing values every 12 days while interpolating the missing values using the K-nearest neighbor (KNN) algorithm. Suppose an LiCSAR deformation dataset is named $D$ in the study area, which includes $N$ deformation maps. To improve the computational speed, $D$ is sampled uniformly, whereas regions with low coherence, such as water bodies and vegetation, will be excluded

$$D_d = D(1 : t : \text{end}) \tag{1}$$

where $D_d$ denotes the deformation map after downsampling, $t$ is the sampling parameter, and $t$ means that one data point is retained for every $t$ original data point in each row/column. This article uses the KNN algorithm for time series missing value checking (12-day interval) and time series interpolation. KNN is a machine learning algorithm that finds several historical data points with the most similar data near the missing points and interpolates the missing values. Compared with ordinary linear interpolation, the advantages of the KNN interpolation method are simplicity and ease of use, fast model training time, and good prediction results.

2) *Anomalous deformation detection module*. This module uses the LSTM anomaly detection technique to model the MTInSAR time series deformation data to screen out anomalous deformation. LSTM is a special kind of

recurrent neural network [35] that solves the gradient disappearance [36], [37] and gradient explosion problems [38] during the training of long sequences. LSTM can dynamically model time series data to achieve more accurate predictions [39], [40]. If the training set of a pixel on $D_d$ is $(D_1^t, D_2^t, \ldots, D_j^t)$ and the corresponding LSTM reconstruction set of that pixel is $(R_1, R_2, \ldots, R_j)$, the reconstruction error at each moment can be expressed as follows:

$$E_j^r = D_j^t - R_j \tag{2}$$

where $E_j^r$, $D_j^t$, and $R_j$ are the reconstruction error, MTInSAR deformation, and reconstruction deformation of the pixel at the moment $j$, respectively.

Since the standard deviation reflects the dispersion of a data set, the standard deviation of the reconstruction error of the training set will be used as an essential indicator for anomaly detection

$$\sigma = \sqrt{\frac{\sum_{i=1}^{j} \left( E_i^r - \overline{E^r} \right)^2}{j}} \tag{3}$$

where $\sigma$ is the standard deviation of the reconstruction error of the training set, and $\overline{E^r}$ is the average reconstruction error of the training set.

Assuming that the validation set for a pixel on $D_d$ is $(D_1^v, D_2^v, \ldots, D_k^v)$ and the corresponding LSTM prediction set for that pixel is $(P_1, P_2, \ldots, P_k)$, the detector will flag a pixel with a prediction error above a threshold as an abnormal deformation

$$|E_k^p| = |D_k^v - P_k| > \sigma \times N_m \tag{4}$$

where $E_k^p$, $D_k^v$, and $P_k$ are the prediction error, deformation verification value, and predicted deformation of the pixel at the moment $k$, respectively, and $N_m$ is a positive integer, which needs to be set in advance by the user based on experience.

3) *Seismic deformation detection module.* Based on the outlier characteristics of seismic deformation in space and time, this module checks the anomalous deformation in time and space, respectively, to output the seismic deformation that meets the outlier characteristics.

Assuming that the number of pixels with abnormal deformation at each moment of the validation set is $(C_1^a, C_2^a, \ldots, C_k^a)$, the moments that exceed the threshold of abnormal deformation can be filtered out according to the following formula:

$$C_k \geq N_a = \frac{A_s}{A_p \times t^2} \tag{5}$$

where $C_k$ is the number of pixels with abnormal deformation at the moment $k$, $N_a$ is the abnormal deformation threshold, $A_s$ is the area of seismic deformation ($A_s$ needs to be set in advance by the user based on experience), $A_p$ is the area of pixels, and the resolution of LiCSAR products is $100 \times 100$ m.

Next, the detector will perform further detection for moments when the threshold is exceeded. Abnormally deformed pixels on the deformation map will be marked as "1," and customarily deformed pixels will be marked as "0." If the edges of the pixels marked with "1" touch each other, these pixels are considered by the detector to be connected, and the detector will consider them to be part of the same object. The detector then counts the number of "1" pixels in each object, and objects with more than $N_a$ are considered by the detector to be "anomalies" caused by seismic deformation. Finally, the actual seismic deformation $D_k^s$ can be calculated by the following equation:

$$D_k^s = D_k^v - P_k. \tag{6}$$

## B. Study Area and Data Set

The phase gradient of the wrapped phase image is more suitable for deformation detection because it is more accessible [41]. However, seismic activity is characterized by uncertainty and the distribution of anomalous pixels is also uncertain. In most cases, it is difficult to distinguish between normal and seismic-associated anomalous deformation signals, making the detection of seismic activity even more challenging. Given that seismic events are rare events in long time series, this article outputs simulated deformation by learning the long-term deformation trend of pixels. If the simulated trend deviates from the actual deformation, the deformation will be judged as anomalous by the detector. As the phase variation is periodic with a period of $2\pi$, the phase restarts and cycles every time the variation exceeds $2\pi$. To reduce the difficulty of model learning and improve the stability of predictions, it is necessary to extract accurate long-term deformation time series data from the study area. Therefore, the unwrapped interferogram is used for phase unwrapping, which corresponds the phase to linear terrain information, thus solving the problem of $2\pi$ ambiguity. As the unwrapping process introduces unwrapping errors, the

"normal" mode in this article is composed of seasonal deformation, orbital error, atmospheric error, unwrapping error, and other "disturbance" signals. Deformation that deviates from the "normal" mode will be regarded as anomalous by the detector.

The LiCSAR product was created using SBASInSAR technology and Sentinel-1 SAR data. The LiCSAR online portal (https://comet.nerc.ac.uk/comet-lics-portal/) provides unwrapped interferograms and coherence estimates. Researchers can use scripts to automatically download unwrapped interferograms and convert unwrapped interferograms to deformations [42]. In this article, the study area is the Mengyuan region of China [see Fig. 3(a)]. The LiCSAR products of ascending and descending tracks in this region are downloaded [see Fig. 3(b)]. The time frame for the ascending track is from January 31, 2017 to January 17, 2022 (152 moments) and the time frame for the descending track is from March 25, 2017 to January 10, 2022 (147 moments). In this article, we construct an LSTM-based neural network for LiCSAR to predict the deformation of image elements [43]. The optimizer algorithm uses the Adaptive moment estimation (Adam) algorithm [44]. Compared with other stochastic optimization methods, the Adam algorithm has the advantages of low hardware resource consumption and the ability to calculate adaptive learning rates for different parameters. Experiments have shown that the Adam algorithm's overall performance is excellent in many practical applications. The network search algorithm is used to compute the optimal hyperparameters with the minimum mean square error loss function as the optimization objective, given the number of network layers K, the number of hidden layer nodes S, and epochs. The maximum range of network layer maximum Kmax and hidden layer node maximum Smax in network search needs to be set by human experience based on the prediction effect. According to the actual training situation, it is sufficient to find the optimal parameters when Kmax and Smax are set to 5 and 30, respectively. Epoch is not as large as possible but generally set to 50–200. The more diverse the data, the larger the corresponding epoch. In this article, the epoch is 200.

The northeastern part of the Qinghai-Tibet Plateau is one of China's most seismically active regions. Many strong earthquakes have occurred in the northeastern part of the Qinghai-Tibet Plateau throughout history, including the 8.5 magnitude earthquake in the Haiyuan fault zone in 1920 and the 7.3 magnitude earthquake that occurred in the Lenglongling fault in 1954 [45], [46], [47]. Geomorphologically, the Menyuan area belongs to the Qaidam Basin. The Qaidam Basin is geotectonically a part of the Qinling Kunlun Qilian trough fold system and is a Miocene depression basin. Since the Tertiary, the Qaidam Basin has been slowly rising, forming a hilly belt composed mainly of Tertiary and Lower and Middle Pleistocene sandstones. The southern part of the Qaidam Basin, which has sunk sharply, is the leading accumulation site of the Quaternary System, up to 1200 m thick, forming a premountain inclined plain composed of the recent flood, alluvial and lacustrine layers of the Upper Pleistocene. The Mengyuan region has high internal stress accumulation and high seismic hazards. An earthquake of magnitude Mw 6.7 hit the Menyuan area on January 8, 2022 [see Fig. 3(c)], and thus can be used to test LADSDIn.
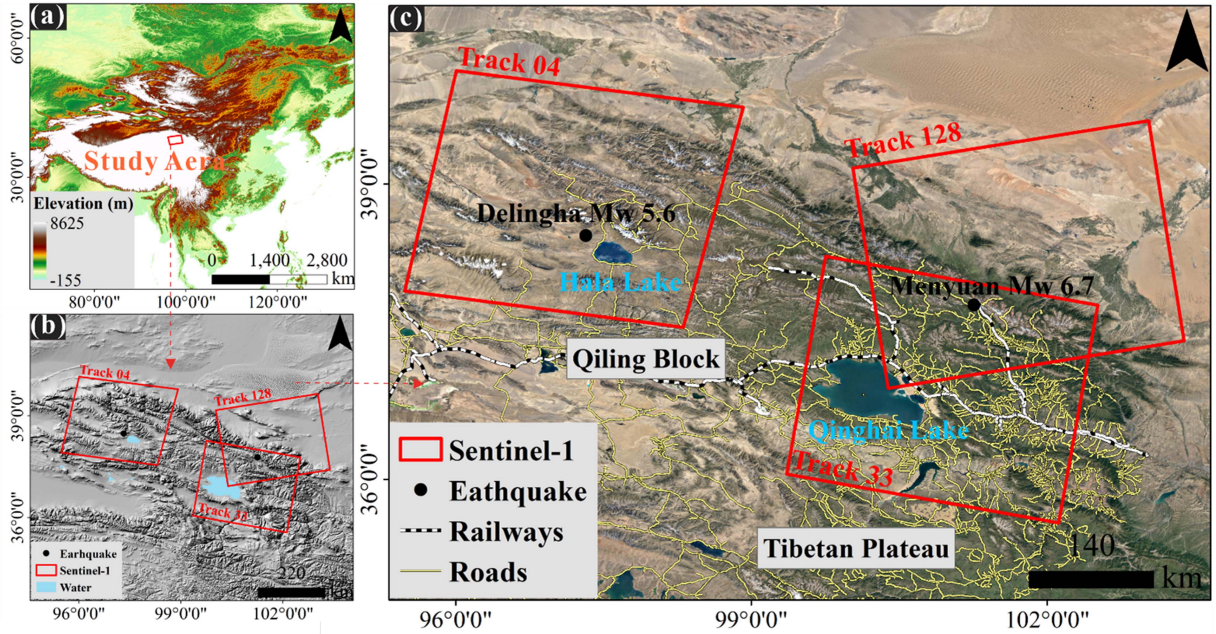
Fig. 3.    Overview of the study area. (a) Geographic location. (b) Topography. (c) Google Earth images.

## III. RESULTS AND ANALYSIS

### A. Abnormal Deformation Detection

Rouet-Leduc et al. [48] predicted the time series deformation trend of InSAR, and their method is similar to the one in this article in some aspects. Still, their model does not know whether the deformation is abnormal. Based on CNN image reconstruction, Deng et al. [45] detected the 2019 Turkey 5.7 magnitude earthquake. The core idea of Deng et al. is to encode the normal input images and train the neural network to learn the distribution patterns of the normal images. The method in this article predicts the future direction of deformation by learning the trend of long time series deformation of pixels, and the deformation that deviates from the prediction is considered an anomaly.

Regarding probability, the small number of earthquakes in a long time series makes seismic detection more suitable for time series anomaly detection. The method in this article does not label the samples, and the anomalies are discriminated in this article based on outlier features of seismic deformation in time and space. This idea facilitates the extraction of seismic-associated abnormal deformation signals.

The values $N_m$ in (4) and $A_s$ in (5) can be determined by looking at historical earthquakes in the surrounding area. Taking the 2021 Mw7.4 earthquake close to the study area as an example, the deformation area of the epicenter is about 1800 km², the deformation of the epicenter is about 1 m, and the normal deformation far from the epicenter is about 0.1 m. The deformation of the epicenter is about ten times the normal deformation [49]. The deformation area of the epicenter of another 2020 Mw 6.6 earthquake is about 600 km², and the deformation of the epicenter is about 0.5 m. The normal deformation far from the epicenter is about 0.1 m, and the epicenter deformation is about

TABLE I
BASIC INFORMATION ON THE DEFORMATION DATA OF THE ASCENDING AND DESCENDING TRACKS

| Track | Ascending | Descending |
|---|---|---|
| Coverage | 97575 km² | 108561 km² |
| Downsampled pixels | 6520 | 5494 |
| Number of monitoring | 152 | 147 |
| Percentage of the training set | 85% | 85% |

five times the normal deformation [50]. Since the earthquake to be detected in this article is an Mw 6.7 earthquake, $N_m$ in (4) is set to 6, $A_s$ in (5) is set to 600 km², and the sampling parameter $t$ is set to 30 in this article.

The Mengyuan earthquake is divided into two comparison experiments, one for the ascending track and one for the descending track, and the parameters are the same for both experiments. In the experiments, 85% of the time series deformation is selected as the training set, and the rest of the data is used as the validation set. The detector samples the ascending and descending tracks separately and uniformly to obtain the time series deformation of each image element. For each image element of the ascending track, the deformations acquired during 2017-01-31 and 2021-04-16 are used as the training set, and those obtained during 2021-04-28 and 2022-01-17 are used as the validation set. For each image element of the descending track, the deformations acquired during 2017-03-25 and 2021-04-21 are used as the training set and those obtained during 2021-05-03 and 2022-01-10 are used as the validation set. After the data cleaning module, the time series deformation of 6520 ascending track pixels and the time series deformation of 5494 descending track pixels were successfully extracted (see Table I).
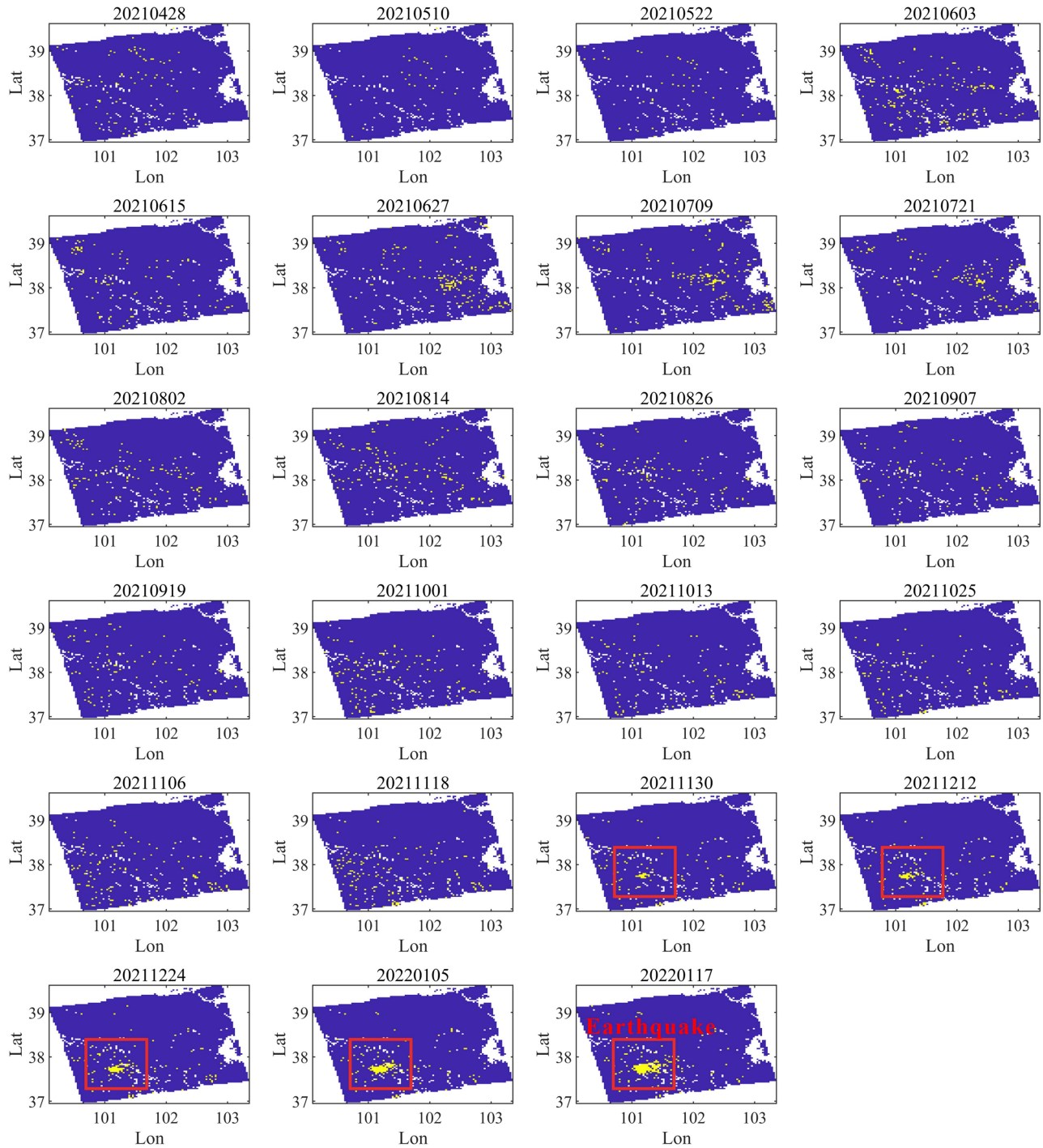
Fig. 4.    Anomalous deformation detection results for the validation set of the ascending track.

The deep learning anomaly detection technique is used to detect the abnormal deformation of the cleaned data. The detection results are shown in Figs. 4 and 5. Blue indicates normal deformation, and yellow indicates abnormal deformation. As can be seen from Fig. 4, in the ascending track data, from April 28, 2021 to November 18, 2021, the anomalous deformation pixels in the study area show a sporadic distribution. From November 30, 2021 to January 17, 2021, an increasing number of anomalous deformation pixels began to be detected in the epicenter area of the Mengyuan earthquake, and the total

number of anomalous deformation pixels reached the maximum on January 17, 2021. It can be found that the evolution of the anomalous deformation of the ascending track coincides with the moment of the Menyuan earthquake (January 8, 2022). As can be seen from Fig. 5, in the descending track data: due to the high number of missing data from May 2021 to August 2021 and the accumulation of errors caused by multiple KNN interpolations, it can be found that the detection results of the descending track data from May 2021 to August 2021 are significantly affected, i.e., a large number of anomalous deformation pixels are detected
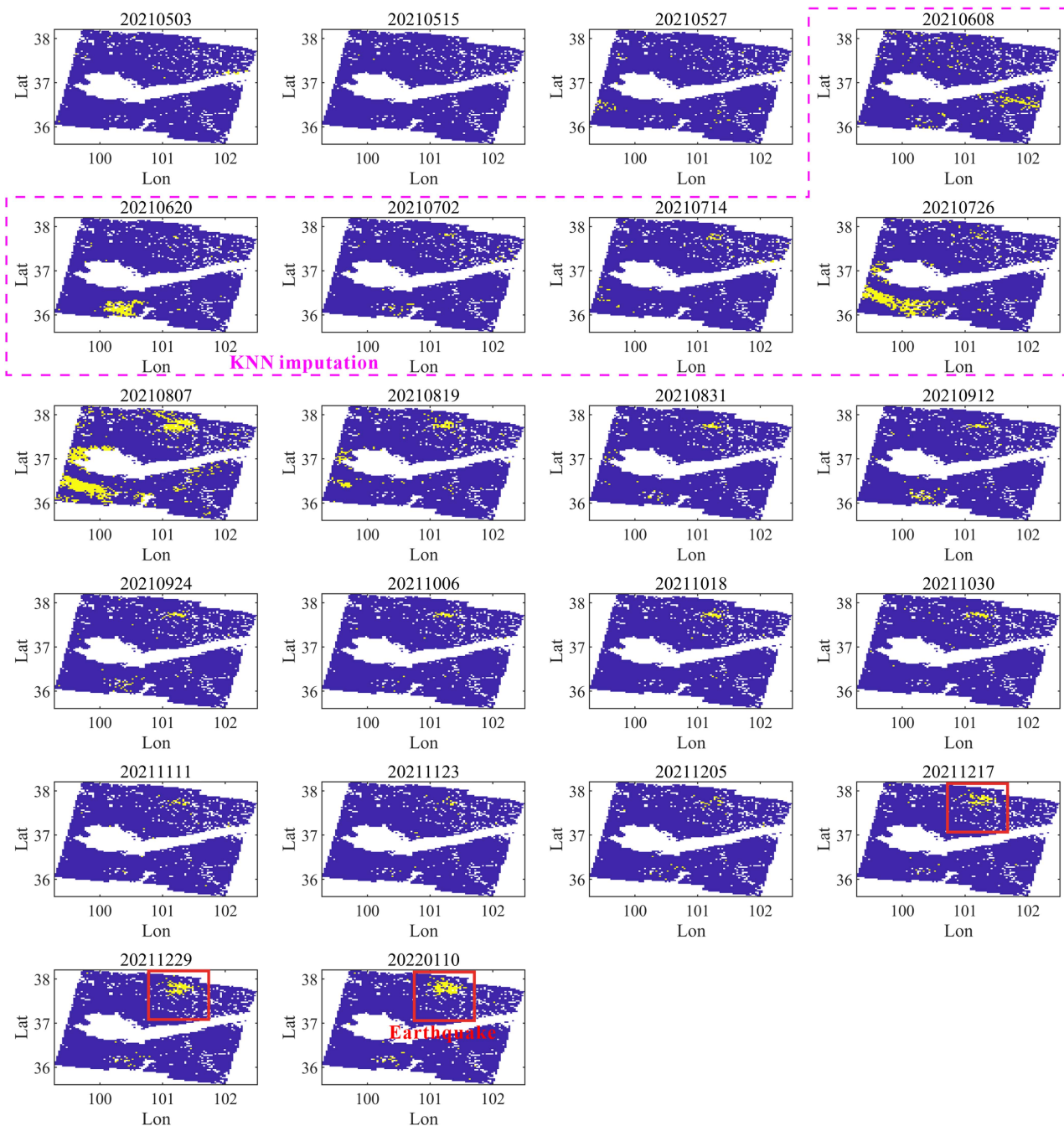
Fig. 5.    Anomalous deformation detection results for the validation set of the descending track.

on August 7, 2021. It was verified that no earthquake occurred at these moments. It is thus clear that the anomalous deformation detection results after multiple interpolations of KNN may not be accurate. The KNN algorithm works by identifying k samples in the time series dataset that are similar in time and then using these samples to estimate the values of the missing data points. Therefore the more consecutive missing values, the more the KNN consecutive interpolated values may gradually deviate from the actual values. Since five consecutive deformation maps were missing between May 27, 2021 and August 7, 2021, all five deformation maps within the red dashed line in Fig. 5 were automatically generated by KNN. In this case, the gap between the KNN predicted and actual values will gradually accumulate, leading to the detection of many anomalies on August 7, 2021. The anomaly on August 7, 2021 is caused by too many consecutive missing deformation maps and excessive KNN interpolations from May 27, 2021 to August 7, 2021. From December 17, 2021 to January 10, 2022, a similarly large number of anomalous deformation pixels were detected in the epicenter region of the Mengyuan earthquake, and the anomalous deformation evolution changes in the descending track data were consistent with the ascending track data.

The anomalous deformation pixels for each moment of the ascending and descending tracks are counted, and the statistics are
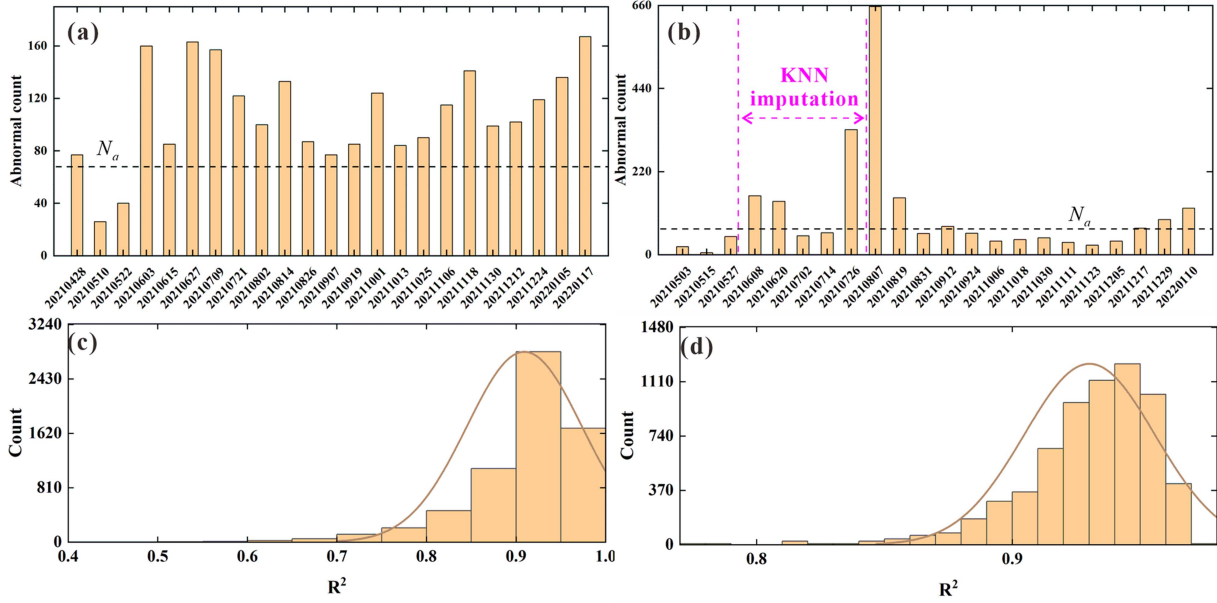
Fig. 6. (a) Anomalous deformation counts for each moment of the validation set of the ascending track. (b) Anomalous deformation counts for each moment of the validation set of the descending track. (c) Determination coefficient statistics for the training set of the ascending track. (d) Determination coefficient statistics for the training set of the descending track.

shown in Fig. 6(a) and (b). Fig. 6(a) shows that the moment with the most anomalous deformation pixels in the ascending track is January 17, 2022 with 167 anomalous deformation pixels detected by the detector. Fig. 6(b) shows that the moment with the most strange anomalous deformation pixels in the descending track is August 7, 2021 with 657 anomalous deformation pixels detected by the detector. The detection results of the descending track are too different from other moments. KNN time series interpolation of random missing values is better than ordinary linear interpolation, but KNN tends to introduce errors when continuous missing is encountered. KNN fills in the missing values by finding a few historical data points similar to the nearby data. The difference between the predicted and actual values of KNN accumulates with the increase of successive missing values. Continuous interpolation causes the expected value to deviate from the actual value gradually, and this "deviation" may be flagged as an "anomaly" by the detector. Such "anomalies" are not anomalous deformations but are caused by the continuous absence of time series deformation maps. It is presumed that the absence of data for May 2021 to August 2021 and the effect of multiple KNN interpolations influenced the detection results for this period.

Five consecutive deformation maps were missing from May 27, 2021 to August 7, 2021, and KNN automatically generated these missing deformation maps in the subsequent processing. Since KNN is predicted concerning the data before and after the lost date, the more consecutive missing values in the time series, the easier it is to gradually cause the expected value to deviate from the actual value. For periods with too many consecutive missing dates, skipping these times can be considered in subsequent studies to improve detector performance. In addition, the coefficient of determination ($R^2$) is used to evaluate the accuracy of the LSTM training set. The value of $R^2$ ranges from 0 to 1. The closer $R^2$ is to 1, the better the model's accuracy. The statistical results show that the average $R^2$ of the ascending track data is 0.90 [see Fig. 6(c)], and the average $R^2$ of the descending track data is 0.93 [see Fig. 6(d)], indicating the modeling accuracy of LSTM is good and can meet the application requirements.

### B. Seismic Deformation Detection

The value $A_s$ in (5) is estimated concerning historical earthquakes in the surrounding area: the seismic deformation area of the 2020 Mw 6.6 earthquake is much larger than 600 km$^2$ [50]. Since the quake to be detected in this article is an Mw 6.7 earthquake, setting $A_s$ in (5) to 600 km$^2$ is sufficient to detect this earthquake. The resolution of the LiCSAR product is 100 × 100 m, the sampling parameter $t$ is 30, and the abnormal deformation pixel threshold is 67, according to (5). The abnormal pixel detection is performed for moments that exceed the anomalous deformation pixel threshold, and the pixel statistics of the maximum anomalous objects for each moment of the validation set are shown in Fig. 7. The moments not involved in anomalous pixel detection are set to 0. In the ascending track data, the abnormal deformation on January 17, 2022 exceeds the threshold [see Fig. 7(a)]. In the descending track data, there are five moments when the anomalous deformation exceeds the threshold, namely June 20, 2021, July 26, 2021, August 7, 2021, December 29, 2021, and January 10, 2022 [see Fig. 7(b)]. From the previous analysis, it is clear that the detection results from May 2021 to August 2021 are erroneous detections caused by more missing descending track data and multiple KNN interpolations, so the results for these dates are excluded. Fig. 8 gives the final seismic deformation extraction results for the two tracks. The results show that the seismic deformation at the epicenter was successfully detected for both tracks, with
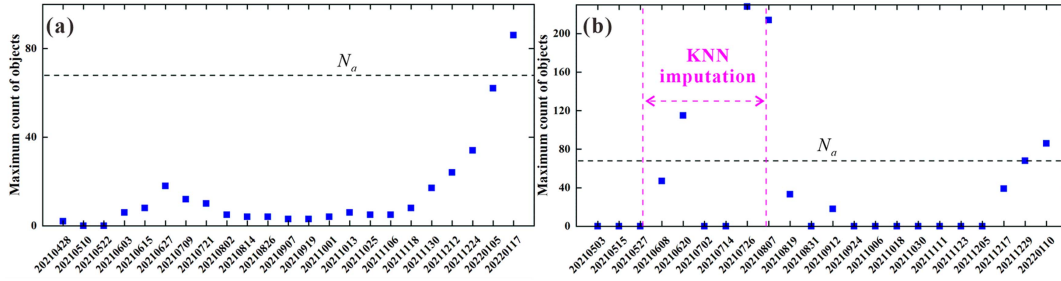
Fig. 7.    Pixel statistics of the maximum anomalous objects at each moment of the validation set. (a) Ascending track. (b) Descending track.
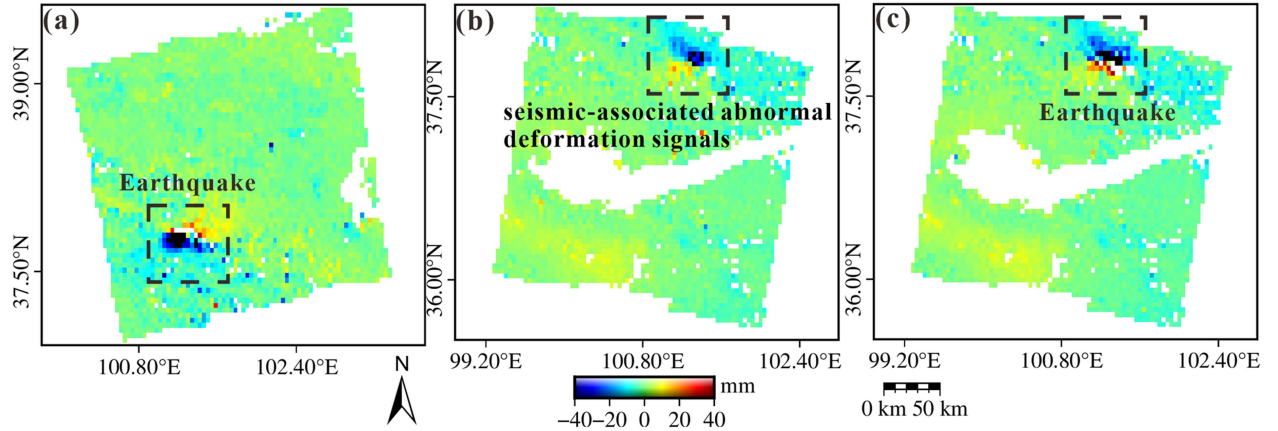


Fig. 8.    Seismic deformation extraction results (line-of-sight direction). (a) January 17, 2022 (ascending track). (b) November 29, 2021 (descending track). (c) January 10, 2022 (descending track).

the deformation range of $-350$ to $87$ mm for the ascending track [see Fig. 8(a)] and $-127$ to $132$ mm for the descending track [see Fig. 8(c)]. Since the inhomogeneous deformation of the ground surface in the epicenter before the earthquake is already very obvious. It can be found that November 29, 2021 (descending track) is recognized by the detector as seismic deformation [see Fig. 8(b)]. This phenomenon suggests that the seismic deformation may have been dominated by horizontal movement and showed pre-earthquake symptoms before the eruption (November 2021). The above analysis concludes that the Mw 6.7 magnitude earthquake that occurred in Mengyuan on January 8, 2022 should be a strike-slip fault-type earthquake with apparent precursors.

The comparison experiments of ascending and descending tracks show that LADSDIn can effectively detect the seismic deformation caused by the Mw 6.7 magnitude earthquake on January 8, 2022 at the door source. The downward trajectory leads to false detection from May 2021 to August 2021 due to missing data at some moments. This problem can be solved by increasing the time interval, e.g., the training interval of the data is changed from 12 days to 48 days. The detector marks November 29, 2021 (descending track) as a seismic deformation, presumably due to the small value of $A_s$ and the significant value of $t$ for the descending track in the experiment. The Mw 6.7 magnitude earthquake in Mengyuan on January 8, 2022 was a strike-slip fault-type earthquake with a significant degree of slip at the epicenter before the earthquake, leading to easy

misinterpretation by detectors as seismic deformation. In addition, most earthquakes are usually transient, and the "abnormal" deformation is more pronounced than the "normal" deformation, so the accuracy of LADSDIn is theoretically better. Overall, the seismic deformation extraction results of both track data are promising, indicating that the seismic deformation detection results of LADSDIn are accurate.

### C. Analysis of Time Series Anomalous Activity of the Mengyuan Earthquake

To study the evolution of the Mw 6.7 magnitude earthquake in Mengyuan on January 8, 2022 and to further elaborate the anomaly detection mechanism of LADSDIn for a single pixel, the time series deformation of the pixel at the source [ascending track, the location of the earthquake source is shown in Fig. 3(c)] is extracted and analyzed in this article. Fig. 9(a) shows the results of comparing the training set deformation and the reconstructed deformation. From Fig. 9(a), it can be found that the random fluctuations eliminated to some extent by the reconstructed deformation can extract the direction of events with seasonal trends. The reconstructed deformation obtained based on LSTM can appropriately represent seasonal deformation's peak and trough changes. Fig. 9(b) shows the correlation between the training set deformation and the model deformation. $R^2$ reaches 0.91, indicating that the model has good feature learning ability and can simulate the deformation
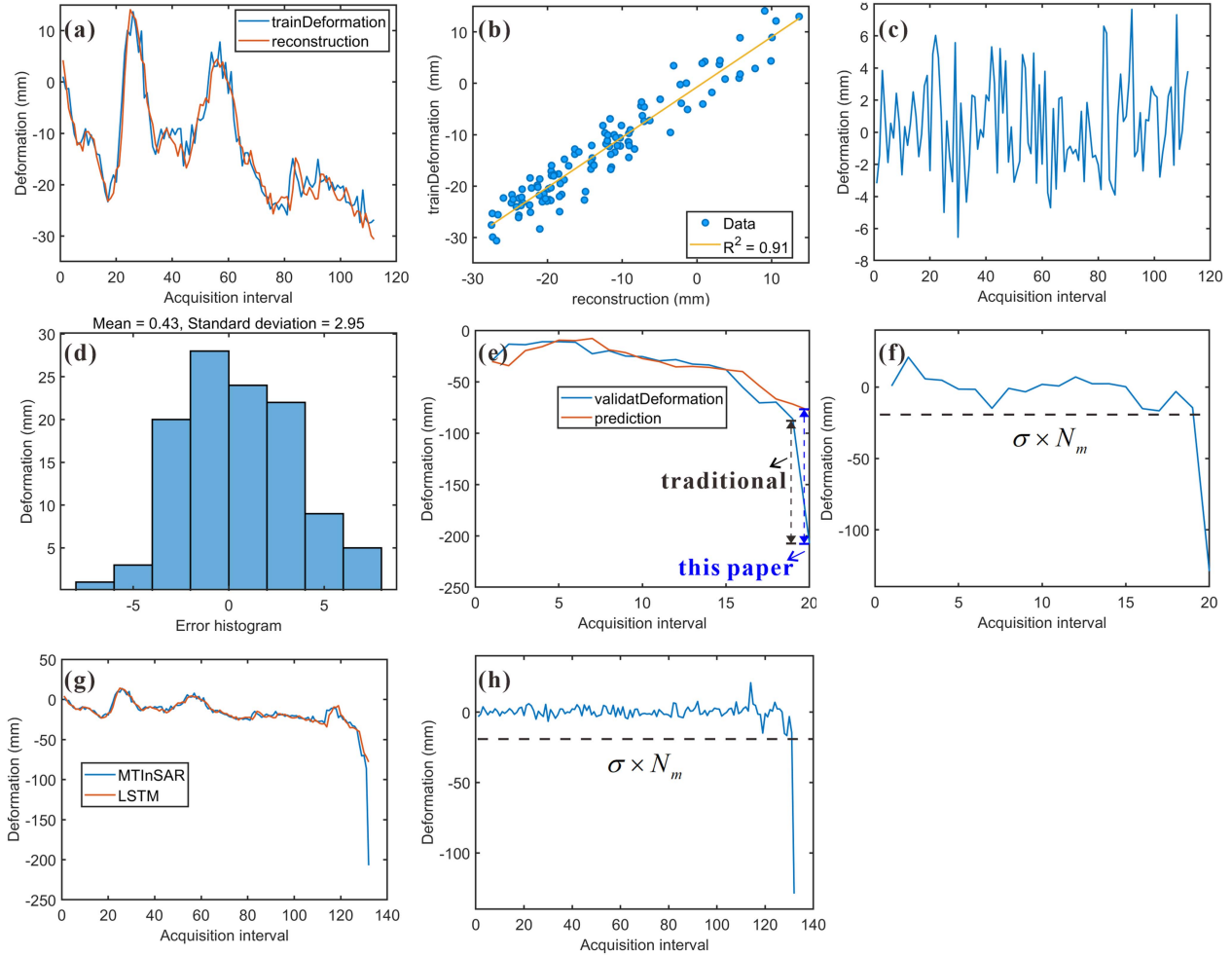
Fig. 9. Time series anomalous activity analysis of pixels at the source. (a) Training set deformation and model deformation. (b) Correlation between training set deformation and model deformation. (c) Reconstruction error of training set. (d) Standard deviation distribution of reconstruction error of training set. (e) Validation set deformation and prediction deformation. (f) Standard deviation distribution of reconstruction error of validation set. (g) MTInSAR deformation and LSTM deformation. (h) Reconstruction error of MTInSAR deformation and LSTM deformation.

trend of the study area more thoroughly. Fig. 9(c) shows the reconstruction error of the training set. From Fig. 9(d), it can be seen that the reconstruction error of this pixel is mainly concentrated in -8 to 8 mm. Fig. 9(d) shows the training set's standard deviation distribution of the reconstruction error. The mean reconstruction error is 0.43 mm with a standard deviation of 2.95 mm, as shown in Fig. 9(d). According to (4), the abnormal deformation threshold for this pixel is 17.7 mm. Fig. 9(d) shows the validation set deformation and the predicted deformation. It can be found that the deformation trends of the validation set deformation and the predicted deformation are almost the same for most of the time until the deviation of the predicted deformation from the validation set deformation starts to increase before the Mw 6.7 earthquake in Mengyuan on January 8, 2022 and then exceeds the threshold of "normal." This phenomenon occurs because the deformation results in the "normal" mode extracted by MTInSAR containing actual deformation signals, atmospheric ones, and other harmful signals [51], [52]. However, the deformation results monitored by MTInSAR after an earthquake contain seismic deformation, actual deformation (usually

seasonal deformation [48]), atmospheric, and other harmful signals. There are few dates of earthquake occurrence in the long-range data, leading the detector to learn data features that do not contain earthquake deformation [see Fig. 9(g)]. When an earthquake occurs, the deviation of the validation set from the predicted value increases dramatically [see Fig. 9(f) and (h)], and this "anomaly" is the "seismic deformation" caused by the earthquake. According to (6), the deformation at the source of the earthquake is −128.98 mm. From the previous analysis, we can see that the seismic deformation results in this article are theoretically closer to the actual seismic deformation because the predicted values of LSTM are subtracted, which is equivalent to further excluding the deformation results in the "normal mode" (actual deformation, atmospheric, and other harmful signals).

### D. Analysis of the Performance and Applicability of the Detector

The experiment used a laptop computer with an AMD Ryzen 7 5800H CPU, 16 GB of running memory, and an NVIDIA

GeForce RTX 3050 Laptop GPU with 4 GB of video memory as the test machine. LADSDIn supports parallel processing in chunks (see Fig. 2). Since the memory capacity of the test machine is only 4 GB, each copy of data is divided equally into eight data blocks to perform parallel processing. The test machine took about 67 min to process the ascending track data (6520 pixels) and about 55 min to process the descending track data (5494 pixels). The current mainstream deep-learning desktop computers have 24 GB of video memory (e.g., RTX 3090). Suppose LADSDIn can be deployed on a computer with 24 GB of video memory. In that case, each copy of data can be further divided into 48 data blocks to perform parallel processing, which is expected to reduce the processing time by about six times.

Traditional seismic deformation extraction requires the manual acquisition of the time and location of the earthquake in advance, followed by processing and analysis of the SAR data, a step that still takes a lot of time. LADSDIn relies on LiCSAR Big Data products, which can detect abnormal deformation in major tectonic zones worldwide and automatically identify and extract seismic deformation. If LADSDIn is deployed on a more powerful server, it may take only a few minutes to examine a set of Sentienl-1 data covering an area of about 100 000 km$^2$. LADSDIn learns the historical characteristics of the data to predict the future, and patterns that deviate from the "expected" are considered anomalies. This novel design model allows LADSDIn to be applied to landslide, collapse, mining, and other scenarios for anomalous deformation detection after modification and parameter debugging.

### E. Supplementary Experiments

The Delingha region experienced an earthquake of magnitude Mw 5.6 on January 23, 2022 [see Fig. 3(c)] and thus can be used to test LADSDIn further. This article uses scripts to automatically download and generate LiCSAR descending track deformation maps for the Delingha region [42]. The time range of LiCSAR descending track deformation maps is January 12, 2019 to January 2, with 90 deformation maps. The data for May 12, 2019, May 24, 2019, July 23, 2019, and July 24, 2021 are missing, so the missing deformation maps are automatically generated using KNN. Experimentally, 85% of the data were selected as the training set, and the remaining data were used as the validation set. Namely, the deformation maps from January 12, 2019 to August 17, 2021 were used as the training set, and the deformation maps from August 29, 2021 to February 1, 2022 were used as the validation set. Zhao et al. [53] showed that the epicenter deformation area of the Mw 5.8 earthquake was 2–4 km$^2$, the epicenter deformation was about 0.3 m, and the normal deformation away from the epicenter was about 0.1 m. The epicenter deformation was nearly three times the normal deformation. In this section, we want to detect seismic deformation in the Delingha region greater than Mw 5.6, so we set $\sigma$ in (4) to 3, b in $A_s$ to 2 km$^2$, the sampling parameter $t$ to 10, and the abnormal deformation pixel threshold is 20 according to (5). The configuration environment of the test machine is the same as the previous experiment.

After the data cleaning module, the temporal deformation of 5021 pixels was successfully extracted. The results of the

detection in the Delingha region are given in Fig. 10, where the detector took about 49 min to process the descending orbit data (5021 pixels). As Fig. 10(a), the detector successfully detected the seismic deformation of the Mw 5.6 earthquake in the Delingha region after January 23, 2022 (February 1, 2022) and the seismic-associated abnormal deformation signals (September 22, 2021 to November 21, 2021). Fig. 10(b) shows the coefficient of determination statistics for the training set of the Delingha experiment. The average $R^2$ of the descending track data reaches 0.78, indicating that the modeling accuracy of LADSDIn is well. In addition, by comparing Figs. 10(a), (c), and (d), a higher number of anomalous deformation pixels were detected in the study area around October 4, 2021, and these anomalous deformation pixels mostly showed a sporadic distribution. On October 4, 2021, the detector detected 100 anomalous deformation pixels from the study area [see Fig. 10(c)]. It detected a large area of abnormal deformation in the northeastern part of the study area [see Fig. 10(a)], probably caused by the pre-earthquake plate motion and the influence of lake water. On July 9, 2021, the anomalous deformation pixels in the study area stabilized until an Mw 5.6 earthquake occurred in the Delingha region on January 23, 2022 [see Fig. 10(d)].

The earthquake of Mw 5.6 magnitude in Delingha occurred on January 23, 2022. Supplementary experiments showed that the detector successfully detected the seismic-associated abnormal deformation signals before the earthquake and the seismic deformation after the quake. The analysis in this section demonstrates that LADSDIn can be successfully applied to another earthquake.

## IV. DISCUSSION

The calculation of seismic deformation fields using DInSAR is a post-earthquake, passive, seismic event-related method. When an earthquake occurs, professional seismic stations use water level meters, seismometers, electromagnetic wave meters, and other equipment to discover the location of the earthquake source. Based on the source location information released by seismic stations, researchers use DInSAR technology and SAR images taken by satellites after the earthquake to calculate the ground deformation at the source. Then, researchers estimate and analyze the geometric parameters of the earthquake based on the ground deformation. Therefore, the calculation of ground deformation using DInSAR is usually a post-earthquake effort. Moreover, the DInSAR method is more challenging to achieve the work of abnormal deformation detection before an earthquake without manual operation.

The method in this article is an active, automatic learning, event-independent anomaly detection. The way in this article can automatically detect anomalous deformation and seismic-associated abnormal deformation signals of LiCSAR data in the tectonic zone. LiCSAR products are produced using SBASInSAR technology and Sentinel-1 SAR data. The products include geocoded unwrapped interferograms and coherence estimates, and researchers can use scripts to automatically download unwrapped interferograms and convert unwrapped interferograms to deformation maps. The advent of LiCSAR Big Data (see Fig. 1) allows us to quickly understand the deformation trends
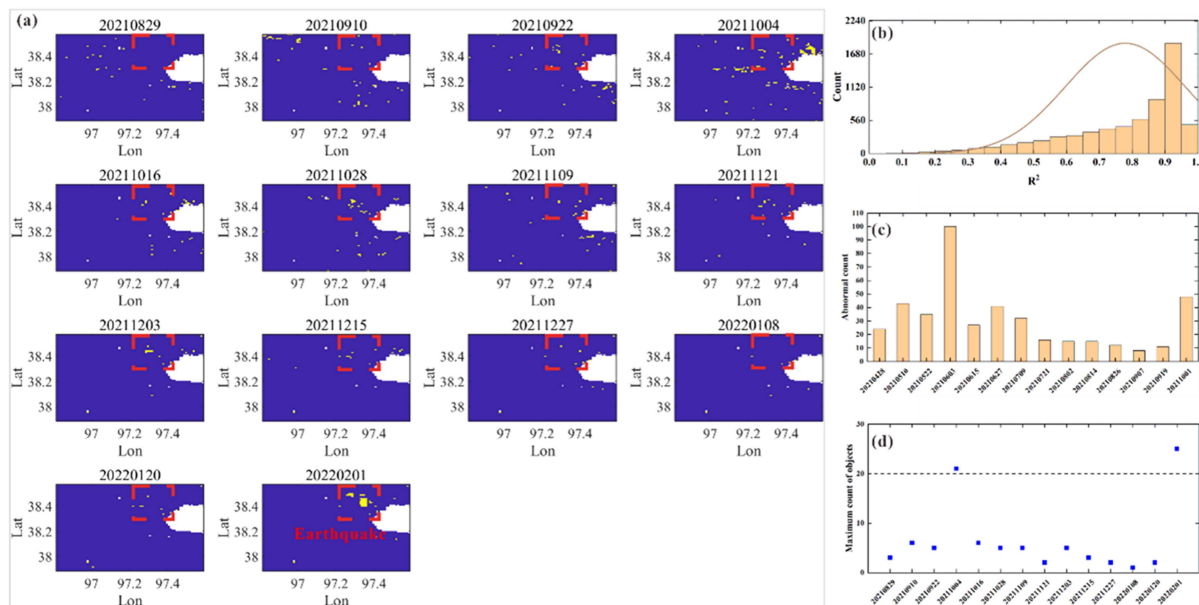
Fig. 10. LADSDIn-based detection results for the Delingha area. (a) Anomalous deformation detection results of the validation set. (b) Determination coefficient statistics of the training set. (c) Anomalous deformation counts for each moment of the validation set. (d) Pixel statistics of the maximum anomalous objects at each moment of the validation set.

in the study area by analyzing historical data. Based on the LiCSAR product, LADSDIn predicts future deformations by learning the deformation characteristics of a long time series of each image element in the study area, and deformations that deviate from the "prediction" are considered abnormal by the detector. Finally, based on the spatial anomalies of seismic deformation, this article uses the "connection" method to detect anomalous elements on a single deformation map and determine whether they are seismic-associated abnormal deformation signals. Therefore, the novelties of this article are the automatic detection of anomalous deformation, automatic detection of seismic-associated abnormal deformation signals, and automatic separation of seismic deformation. Moreover, the focus of this article is more on preseismic data analysis.

In the area where the ground deformation shows periodic changes [see Fig. 2(c)], the seismic deformation extracted by the method in this article will be theoretically closer to the actual seismic deformation than the DInSAR deformation. The DInSAR method is based on the deformation field calculated from two SAR images taken by the satellite before and after the earthquake. This way ignores the deformation trend of the study area itself. As Fig. 2(c), since the ground deformation of the pixel shows periodic changes, if there is no earthquake, we can predict the latest deformation trend based on the historical deformation. However, due to an earthquake's occurrence, the earthquake's ground deformation masks the pixel's deformation trend, resulting in the seismic deformation calculated by DInSAR being smaller than the actual seismic deformation. If we use (6) for the calculation, the above problem can be somewhat avoided.

The time of the Mengyuan earthquake is January 8, 2022. The detection results in this article show that the detector successfully detected seismic-associated abnormal deformation signals before the quake. This work may help the automation and refinement study of seismic activities in China. Mengyuan Mw 6.7 earthquake on January 8, 2022, severely damaged some sections of the Lanzhou–Xinjiang high-speed railway, damaging several tunnels and bridges and interrupting high-speed railway traffic. According to the automatic detection results of the detector (see Figs. 4 and 5), it can be found that seismic-associated abnormal deformation signals have been detected in the gate–source region from November 30, 2021. China is an earthquake-prone country with many seismic zones and a high frequency of earthquakes. However, the current research on earthquake precursors is still unclear, and further research is necessary for ground deformation as the most direct and obvious phenomenon of earthquake occurrence. Therefore, this article's method and detection results may provide sample references for automated and refined studies of seismic activity. In addition, the method in this article not only extracts the historical deformation of the long time series in the study area but also detects the abnormal changes in the historical deformation. The above work can be more convenient for researchers further to analyze the surface activity characteristics before the earthquake.

The local SBAS InSAR method can be used to obtain deformation maps of time series based on unwrapped interferograms and detecting abnormal deformation, but acquiring unwrapped interferograms requires time and effort. LiCSAR is a product processed by a supercomputer, which contains unwrapped interferograms and can help researchers save time by eliminating the need for orbital correction, image registration, interferogram generation, interferogram filtering, and interferogram unwrapping, allowing them to focus more on the application of research.

LiCSAR products cover China's major seismic structural regions, providing convenience for the rapid application of the method proposed in this article in seismic structural regions.

Therefore, it is recommended to prioritize the use of methods based on LiCSAR products, which can quickly obtain long time series deformation data. By studying the deformation maps of long time series, pre-earthquake surface activity anomalies can be detected and further separate real earthquake deformation.

For the full process localization scenario of extracting point targets with large abnormal changes quickly, in future research, it may be useful to consider combining SBAS InSAR with other alternative algorithms. By analyzing the phase changes of interferogram pairs paired at different times, abnormal information can be extracted.

## V. CONCLUSION

Manual analysis of LiCSAR deformation data in tectonic zones and timely detection of pre-earthquake anomalous activity are very time-consuming. To solve this problem, a (LADSDIn) is constructed in this article. The detector predicts future deformations by systematically learning the historical characteristics of the data. Pixels deviating from the "predicted" deformation are considered "abnormal" deformations. The detector learns the unique numerical characteristics of the seismic deformation to determine whether the pixels of the "anomalous deformation" match the seismic characteristics and then separates the seismic deformation. LADSDIn consists of three main modules, i.e., data cleaning module, anomalous deformation detection module, and seismic deformation detection module. The data cleaning module is used to uniformly sample the LiCSAR deformation results and determine whether there are missing values every 12 days while interpolating the missing values using the KNN algorithm. The anomalous deformation detection module uses the LSTM anomaly detection technique to model the MTInSAR time series deformation data and determine the anomalous deformation by calculating the reconstruction error. The seismic deformation detection module improves the accuracy of seismic deformation detection by examining anomalous deformation pixels in time and space based on the temporal and spatial outlier characteristics of seismic deformation and then finding the natural anomalies caused by seismic deformation.

January 8, 2022, the Mengyuan earthquake in China shows that seismic-associated abnormal deformation signals were identified. The results show that the deformation range of the ascending track is $-350$ to $87$ mm, and the deformation range of the descending track is $-127$ to $132$ mm. The detector successfully detected the "anomalous deformation" signs before the earthquake (November 2021). The comparison analysis indicates that the seismic deformation may be dominated by horizontal movement, so it is speculated that the Mw 6.7 earthquake that occurred in Mengyuan on January 8, 2022 should be a slip-fault type earthquake with obvious ground deformation precursors.

Compared with traditional seismic deformation calculation methods, the seismic deformation results in this article are theoretically closer to the actual seismic deformation because the predicted values of LSTM are subtracted, which is equivalent to further excluding the deformation results in "normal mode" (actual deformation, atmospheric, and other harmful signals). In addition, LADSDIn supports parallel processing in chunks, and it may take only a few minutes to analyze a set of Sentienl-1

data covering an area of about 100 000 km$^2$ if LADSDIn is deployed on a more powerful server. This work is significant for the application and study of the refinement of solid earth and natural hazards.

Since LADSDIn learns historical data characteristics to make predictions, patterns that deviate from "expectations" are considered anomalies. This novel design model allows LADSDIn to be applied to landslide, collapse, mining, and other scenarios for anomalous deformation detection after modification and parameter debugging.

## REFERENCES

[1] S. Karimzadeh, M. Ghasemi, M. Matsuoka, K. Yagi, and A. C. Zulfikar, "A deep learning model for road damage detection after an earthquake based on synthetic aperture radar (SAR) and field datasets," *IEEE J. Sel. Topics Appl. Earth Observ. Remote Sens.*, vol. 15, pp. 5753–5765, 2022.

[2] Y. Morishita, "A systematic study of synthetic aperture radar interferograms produced from ALOS-2 data for large global earthquakes from 2014 to 2016," *IEEE J. Sel. Topics Appl. Earth Observ. Remote Sens.*, vol. 12, no. 7, pp. 2397–2408, Jul. 2019.

[3] S. Karimzadeh and M. Matsuoka, "Building damage characterization for the 2016 Amatrice earthquake using ascending–descending COSMO-SkyMed data and topographic position index," *IEEE J. Sel. Topics Appl. Earth Observ. Remote Sens.*, vol. 11, no. 8, pp. 2668–2682, Aug. 2018.

[4] H. N. Shea and W. D. Barnhart, "The Geodetic Centroid (gCent) Catalog: Global earthquake monitoring with satellite imaging geodesy," *Bull. Seismol. Soc. Amer.*, vol. 112, no. 6, pp. 2946–2957, 2022.

[5] D. E. Goldberg, P. Koch, D. Melgar, S. Riquelme, and W. L. Yeck, "Beyond the teleseism: Introducing regional seismic and geodetic data into routine USGS finite-fault modeling," *Seismol. Soc. Lett.*, vol. 93, no. 6, pp. 3308–3323, 2022.

[6] A. Pırtı, R. G. Hoşbaş, and M. A. Yücel, "Examination of the earthquake (Samos Island) in Izmir (30.10. 2020) by using Cors-Tr GNSS observations and InSAR data," *KSCE J. Civil Eng.*, vol. 27, no. 1, pp. 135–144, 2023.

[7] H. A. Zebker, P. A. Rosen, and S. Hensley, "Atmospheric effects in interferometric synthetic aperture radar surface deformation and topographic maps," *J. Geophys. Res., Solid Earth*, vol. 102, no. B4, pp. 7547–7563, 1997.

[8] Z.-F. Ma, S.-J. Wei, Y. Aoki, J.-H. Liu, and T. Huang, "A new spatiotemporal InSAR tropospheric noise filtering: An interseismic case study over Central San Andreas fault," *IEEE Trans. Geosci. Remote Sens.*, vol. 60, 2022, Art. no. 5235016.

[9] R. Lanari et al., "An overview of the small baseline subset algorithm: A DInSAR technique for surface deformation analysis," *Pure Appl. Geophys.*, vol. 164, pp. 637–661, 2007.

[10] R. Lanari, O. Mora, M. Manunta, J. J. Mallorquí, P. Berardino, and E. Sansosti, "A small-baseline approach for investigating deformations on full-resolution differential SAR interferograms," *IEEE Trans. Geosci. Remote Sens.*, vol. 42, no. 7, pp. 1377–1386, Jul. 2004.

[11] A. Ferretti, C. Prati, and F. Rocca, "Nonlinear subsidence rate estimation using permanent scatterers in differential SAR interferometry," *IEEE Trans. Geosci. Remote Sens.*, vol. 38, no. 5, pp. 2202–2212, Sep. 2000.

[12] D. A. Schmidt and R. Bürgmann, "Time-dependent land uplift and subsidence in the Santa Clara valley, California, from a large interferometric synthetic aperture radar data set," *J. Geophys. Res., Solid Earth*, vol. 108, no. B9, 2003, Art. no. 2416.

[13] F. Bovenga et al., "Assessing the potential of long, multi-temporal SAR interferometry time series for slope instability monitoring: Two case studies in Southern Italy," *Remote Sens.*, vol. 14, no. 7, 2022, Art. no. 1677.

[14] G. C. Kothyari et al., "Identification of active deformation zone associated with the 28th April 2021 Assam earthquake (Mw 6.4) using the PSInSAR time series," *J. Appl. Geophys.*, vol. 206, 2022, Art. no. 104811.

[15] P. Confuorto et al., "Sentinel-1-based monitoring services at regional scale in Italy: State of the art and main findings," *Int. J. Appl. Earth Observ. Geoinf.*, vol. 102, 2021, Art. no. 102448.

[16] P. Friedl, T. Seehaus, and M. Braun, "Global time series and temporal mosaics of glacier surface velocities derived from Sentinel-1 data," *Earth Syst. Sci. Data*, vol. 13, no. 10, pp. 4653–4675. 2021.

[17] A. Hooper et al., "Exploiting InSAR on a large scale for tectonics and volcano monitoring," in *Proc. IEEE Int. Geosci. Remote Sens. Symp.*, 2020, pp. 6857–6858.

[18] F. Hu, F. J. Van Leijen, L. Chang, J. Wu, and R. F. Hanssen, "Combined detection of surface changes and deformation anomalies using amplitude-augmented recursive inSAR time series," *IEEE Trans. Geosci. Remote Sens.*, vol. 60, 2022, Art. no. 5210816.

[19] M. Lazecký et al., "LiCSAR: An automatic InSAR tool for measuring and monitoring tectonic and volcanic activity," *Remote Sens.*, vol. 12, no. 15, 2020, Art. no. 2430.

[20] K. D. Murray, R. B. Lohman, and D. P. S. Bekaert, "Cluster-based empirical tropospheric corrections applied to InSAR time series analysis," *IEEE Trans. Geosci. Remote Sens.*, vol. 59, no. 3, pp. 2204–2212, Mar. 2021.

[21] J. F. Fonseca, M. Palano, A. P. Falcão, A. Hrysiewicz, and J. Fernandez, "Interseismic strain accumulation near Lisbon (Portugal) from space geodesy," *Geophys. Res. Lett.*, vol. 48, no. 24, 2021, Art. no. e2021GL096862.

[22] B. Liu et al., "Activity analysis of the fuyu north fault, China: Evidence from the time-series InSAR, GNSS, seismic reflection profile, and plate dynamics," *Lithosphere*, vol. 2022, 2022, Art. no. 2789572.

[23] E. Bayramov, G. Tessari, and M. Kada, "Quantifying two-dimensional surface displacements using high-resolution cosmo-SkyMed, TerraSAR-X and medium-resolution Sentinel-1 SAR interferometry: Case study for the Tengiz oilfield," *Sensors*, vol. 22, no. 17, 2022, Art. no. 6416.

[24] B. Han, C. Yang, Z. Li, C. Yu, C. Zhao, and Q. Zhang, "Coseismic and postseismic deformation of the 2016 Mw 6.0 Petermann ranges earthquake from satellite radar observations," *Adv. Space Res.*, vol. 69, no. 1, pp. 376–385, 2022.

[25] A. Fathian et al., "Complex co- and postseismic faulting of the 2017–2018 seismic sequence in western Iran revealed by InSAR and seismic data," *Remote Sens. Environ.*, vol. 253, 2021, Art. no. 112224.

[26] M. Lazecky et al., "Sentinel-1 InSAR data by LiCSAR system," EGU General Assembly, EGU21-2929, 2021.

[27] M. Lazecky et al., "Updates on the COMET LiCSAR system for automatised global interferometric measurements of tectonic and volcanic areas using Sentinel-1 InSAR data," in *Proc. AGU Fall Meeting*, G34A-05, 2021.

[28] M. Lazecky, Y. Maghsoudi, F. Albino, A. J. Hooper, and T. J. Wright, "Improvements in the licsar generator of Sentinel-1 interferograms," in *Proc . IEEE Int. Geosci. Remote Sens. Symp.*, 2021, pp. 2671–2674.

[29] W. Sun, Z. Wei, H. Sun, and H. He, "Review on the application of airborne LiDAR in active tectonics of China: Dushanzi reverse fault in the Northern Tian Shan," *Front. Earth Sci.*, vol. 10, 2022, Art. no. 895758.

[30] H. Chen, "Overview of the seismic input at dam sites in China," *Earthq. Sci.*, vol. 35, no. 5, pp. 410–425. 2022.

[31] L. Wang, M. Chang, J. Le, L. Xiang, and Z. Ni, "Two multi-temporal datasets to track debris flow after the 2008 Wenchuan earthquake," *Sci. Data*, vol. 9, no. 1, 2022, Art. no. 525.

[32] P. Wang, E. Fan, and P. Wang, "Comparative analysis of image classification algorithms based on traditional machine learning and deep learning," *Pattern Recognit. Lett.*, vol. 141, pp. 61–67. 2021.

[33] A. H. Kashou, A. M. May, and P. A. Noseworthy, "Comparison of two artificial intelligence-augmented ECG approaches: Machine learning and deep learning," *J. Electrocardiol.*, vol. 79, pp. 75–80. 2023.

[34] Y. Pan and L. Zhang, "Mitigating tunnel-induced damages using deep neural networks," *Autom. Construction*, vol. 138, 2022, Art. no. 104219.

[35] S. Hochreiter and J. Schmidhuber, "Long short-term memory," *Neural Comput.*, vol. 9, no. 8, pp. 1735–1780. 1997.

[36] M. Ma, C. Liu, R. Wei, B. Liang, and J. Dai, "Predicting machine's performance record using the stacked long short-term memory (LSTM) neural networks," *J. Appl. Clin. Med. Phys.*, vol. 23, 2022, Art. no. e13558.

[37] Z. Li, H. Gurgel, L. Xu, L. Yang, and J. Dong, "Improving dengue forecasts by using geospatial big data analysis in Google Earth Engine and the historical dengue information-aided long short term memory modeling," *Biology*, vol. 11, no. 2, 2022, Art. no. 169.

[38] X. Chen et al., "A new rainfall-runoff model using improved LSTM with attentive long and short lag-time," *Water*, vol. 14, no. 5, 2022, Art. no. 697.

[39] K. ArunKumar, D. V. Kalaga, C. M. S. Kumar, M. Kawaji, and T. M. Brenza, "Comparative analysis of gated recurrent units (GRU), long short-term memory (LSTM) cells, autoregressive integrated moving average (ARIMA), seasonal autoregressive integrated moving average (SARIMA) for forecasting COVID-19 trends," *Alexandria Eng. J.*, vol. 61, no. 10, pp. 7585–7603, 2022.

[40] X. Bao et al., "Ground deformation pattern analysis and evolution prediction of Shanghai Pudong international airport based on PSI long time series observations," *Remote Sens.*, vol. 14, no. 3, 2022, Art. no. 610.

[41] Y. Shen et al., "Rapid and automatic detection of new potential landslide based on phase-gradient DInSAR," *IEEE Geosci. Remote Sens. Lett.*, vol. 19, 2022, Art. no. 4514205.

[42] Y. Morishita, M. Lazecky, T. J. Wright, J. R. Weiss, J. R. Elliott, and A. Hooper, "LiCSBAS: An open-source InSAR time series analysis package integrated with the LiCSAR automated Sentinel-1 InSAR processor," *Remote Sens.*, vol. 12, no. 3, 2020, Art. no. 424.

[43] Y. Yu, X. Si, C. Hu, and J. Zhang, "A review of recurrent neural networks: LSTM cells and network architectures," *Neural Computat.*, vol. 31, no. 7, pp. 1235–1270, 2019.

[44] K. G. Devi, C. K. Balasubramanian, Senthilkumar, and K. Ramya, "Accurate prediction and classification of corn leaf disease using adaptive moment estimation optimizer in deep learning networks," *J. Elect. Eng. Technol.*, vol. 18, no. 1, pp. 637–649, 2023.

[45] Q. Deng et al., "Variations in the geometry and amount of slip on the Haiyuan (Nanxihaushan) fault zone, China and the surface rupture of the 1920 Haiyuan earthquake," *Earthq. Source Mechanics*, vol. 37, pp. 169–182, 1986.

[46] Z. J. Liu et al., "Millennial recurrence of large earthquakes on the Haiyuan fault near Songshan, Gansu province, China," *Bull. Seismol. Soc. Amer.*, vol. 97, no. 1B, pp. 14–34. 2007.

[47] X. W. Xu, R. S. Yeats, and G. H. Yu, "Five short historical earthquake surface ruptures near the silk road, Gansu province, China," *Bull. Seismol. Soc. Amer.*, vol. 100, no. 2, pp. 541–561. 2010.

[48] B. Rouet-Leduc, R. Jolivet, M. Dalaison, P. A. Johnson, and C. Hulbert, "Autonomous extraction of millimeter-scale deformation in InSAR time series using deep learning," *Nature Commun.*, vol. 12, no. 1, 2021, Art. no. 6480.

[49] M. Lyu, K. Chen, C. Xue, N. Zang, W. Zhang, and G. Wei, "Overall subshear but locally supershear rupture of the 2021 Mw 7.4 Maduo earthquake from high-rate GNSS waveforms and three-dimensional InSAR deformation," *Tectonophysics*, vol. 839, 2022, Art. no. 229542.

[50] H. Gao, M. Liao, X. Liang, G. Feng, and G. Wang, "Coseismic and postseismic fault kinematics of the July 22, 2020, Nima (Tibet) Ms6.6 earthquake: Implications of the forming mechanism of the active N-S-trending grabens in Qiangtang, Tibet," *Tectonics*, vol. 41, no. 3, 2022, Art. no. e2021TC006949.

[51] M. Simons and P. Rosen, "Interferometric synthetic aperture radar geodesy," *Geodesy*, vol. 3, pp. 391–446, 2007.

[52] T. Emardson, M. Simons, and F. Webb, "Neutral atmospheric delay in interferometric synthetic aperture radar applications: Statistical description and mitigation," *J. Geophys. Res., Solid Earth*, vol. 108, no. B5, 2003, Art. no. 2231.

[53] D. Zhao, C. Qu, X. Shan, W. Gong, G. Zhang, and X. Song, "New insights into the 2010 Yushu Mw 6.9 mainshock and Mw 5.8 aftershock, China, from InSAR observations and inversion," *J. Geodyn.*, vol. 125, pp. 22–31, 2019.

**Xianjian Shi** is currently working toward the Ph.D. degree with the School of Remote Sensing and Information Engineering, Wuhan University, China.

His main research interests include ground deformation monitoring.

**Bin Pan** received the B.S. and M.S. degrees in photogrammetry and remote sensing from the Wuhan Technical University of Surveying and Mapping, Wuhan, China, in 1994 and 1999, respectively, and the Ph.D. degree in photogrammetry and remote sensing from Wuhan University, Wuhan, China, in 2010.

From 1994 to 1996, he was a Teaching Assistant with the Department of Aero Photogrammetry, Wuhan Technical University of Surveying and Mapping, where he was a Lecturer till 1999. From 2000 to 2004, he was a Lecturer with the School of Remote Sensing and Information Engineering, Wuhan University, where he was an Associate Professor till 2009 and has been a Professor since 2010. He has coauthored two books and authored or coauthored more than 30 articles, more than 20 inventions, and participated in multiple national high-tech research programs.